ACS Photonics

Article

Cite This: ACS Photonics 2019, 6, 3306−3314

pubs.acs.org/journal/apchd5

Nonlinear Born-Kuhn Analog for Chiral Plasmonics

Lili Gui,*[,†,‡] Mario Hentschel,[†] Josselin Defrance,[†] Joachim Krauth,[†] Thomas Weiss,[†] and Harald Giessen[†]

[†]4th Physics Institute and Research Center SCoPE, University of Stuttgart, Pfaffenwaldring 57, 70569 Stuttgart, Germany

[‡]State Key Laboratory of Information Photonics and Optical Communications, Beijing University of Posts and Telecommunications, Beijing 100876, China

Supporting Information

ABSTRACT: Chiral plasmonic metasurfaces are intriguing platforms to achieve large nonlinear chiroptical effects, which could be desirable for sensitive chiral molecular analysis. The combination of a superlinear response with high plasmonic near-field enhancement leads to large nonlinear optical activity, which can be much stronger than its linear counterpart. A complex mixture of multiresonances, structural symmetry, and anisotropy in 3D chiral plasmonic nanostructures as well as experimental configurations has up to now hampered understanding of the underlying physics and quantitative modeling of the relevant nonlinear chiroptical effects. Here we study third-harmonic circular dichroism of archetypical Born-Kuhn type bilayer chiral metasurfaces made of corner-stacked orthogonal gold nanorods arranged in C_4 symmetry, which avoids most of the aforementioned issues. With a coupled anharmonic oscillator model built upon chirally coupled electric dipole moments, we are able to retrieve the nonlinear chiroptical response of such chiral nanostructures. The comparison of nonlinear spectroscopic measurements with our model as well as nonlinear simulations enables interpretation of the large nonlinear circular dichroism. Our research might pave the way toward flexible control over nonlinear susceptibility tensors of artificial chiral meta-molecules at will and could allow for highly sensitive nonlinear chiral sensing.

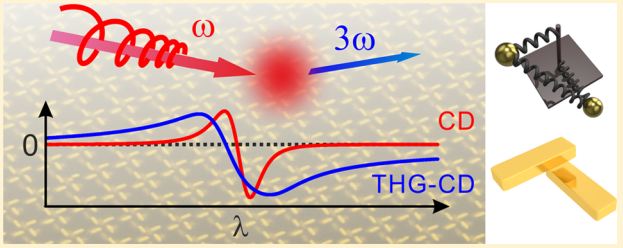

KEYWORDS: *nonlinear optics, chirality, plasmonics, third-harmonic generation, circular dichroism, anharmonic oscillator model*

Objects are called chiral when they cannot be superimposed with their mirror images by simple translation or rotation.[1,2] Chiral biomolecules such as DNA and enzymes exist in both nature and industrial production chains, particularly in biomedicines. Chiral substances can manifest themselves optically, namely by distinct optical response with left- or right-handed circularly polarized light (LCP or RCP). In a homogeneous and isotropic chiral medium, the difference of the imaginary part of the refractive index n under LCP and RCP light yields differential absorbance, the so-called circular dichroism (CD),[3,4] which is detected by CD spectrometer to probe the molecular chirality (left- or right-handedness, LH or RH) together with the concentration of the targeted objects. Chiral plasmonics, which works on 2D or 3D metallic nanostructures, aims to mimic and utilize optical activity in nature,[5,6] design and achieve artificial gigantic chiroptical effects,[7−12] as well as sense chiral molecules with high sensitivity for biological[13] and chemical[14] applications. Indeed, some trials on chiral plasmonic sensing have shown outstanding enantioselective detection performances (yet under debate) and inspired further research.[15−17]

Besides linear optical activity, nonlinear chiroptical response in plasmonic systems has also been studied for several years.[18−24] In comparison to linear chiroptical effects, one could argue that nonlinear counterparts might exhibit larger relative strength, as demonstrated in previous studies on second-order nonlinear optical activity for chiral monolayers and chiral metasurfaces.[19,21,25] Moreover, as a generally intrinsic merit, nonlinear optical effects are superlinearly proportional to the properties of the ambient environment,[26−30] such as the dielectric constant. Both aspects could endow nonlinear optical activity, with the potential for chiral sensing with higher sensitivity.[19,20] Particularly, second-harmonic generation (SHG) is very sensitive to structural symmetry and surface effects.[18,31] SHG-CD, that is, relative differential SHG intensity with LCP and RCP fundamental incident light, has been found to be much more pronounced than linear CD, according to some pioneering experimental reports.[19,32,33] Until now, SHG from different 2D and 3D chiral nanostructures has been intensively explored, for instance, G-shapes,[18] gammadions,[21] twisted arcs,[32] twisted nanocrosses,[19] nanohelices,[34−36] triangular nanoprisms,[22] and so on.

Despite a plethora of research, fundamental understanding and theoretical modeling of SHG-CD in chiral plasmonic structures are still limited, mainly due to the following reasons: First, most of the structures are usually very complex in shape,

Received: September 26, 2019
Published: November 21, 2019

DOI: 10.1021/acsphotonics.9b01400
ACS Photonics 2019, 6, 3306−3314

involving several resonant modes; second, the lattice and structural symmetry as well as experimental configuration can add anisotropy to the systems, which is mixed with chirality; third, SHG is very sensitive to any structural deformation, which is hardly avoidable during fabrication procedures. We have previously demonstrated theoretical modeling and interpretation of linear CD of 3D chiral plasmonic metasurfaces consisting of corner-stacked orthogonal gold nanorods arranged in C_4 symmetry,[3] which mimics Born-Kuhn chiral molecules[37,38] and avoids most of the aforementioned problems. Our structures were fully embedded into a dielectric environment to avoid any spatial asymmetry or surface effects. Here, we build an extended nonlinear Born-Kuhn model that treats plasmons as chirally coupled anharmonic classical oscillators and serves as a quantitative approach to unravel the origin of the nonlinear CD of such purely chiral nanostructures. The structural lattice exhibits C_4 rotational symmetry, which ensures efficient third-harmonic generation (THG) instead of SHG in experiment[39−41] and avoids linear birefringence due to anisotropy. Its THG-CD can be well interpreted under the framework of our analytical expressions. In addition, numerical simulations have been carried out using the Fourier modal method[42] and the reciprocity principle,[43] which give rise to similar linear and nonlinear chiroptical spectra when compared to our measurement. All results prove that the third-harmonic generation in such chiral plasmonic metamolecules strongly depends on the handedness of the pump wave, and the THG-CD can exhibit similar dispersive lineshapes as its linear counterparts, but may possess maximum or minimum values at different spectral positions.

RESULTS AND DISCUSSION

The general concept of our study on the Born-Kuhn-type plasmonic metasurfaces is schematically illustrated in Figure 1a. LCP or RCP light illuminates under normal incidence the periodic arrays consisting of corner-stacked orthogonal gold nanorods (only one supercell is indicated for the sake of clarity). The differential transmittance and THG intensity can be recorded accordingly, which then correspond to CD and THG-CD, respectively. Incident and transmitted waves at the fundamental frequency are indicated in red, while THG waves are indicated in blue. For analytical modeling, we first study two orthogonally coupled nanorods and treat the chirally arranged plasmons as classical oscillators (Figure 1b). Following the original description of chiroptical properties of molecules,[38] we use the highly successful "coupled spring model" to describe the displacement of the electrons, where the oscillator amplitudes are coupled together. Extending the Born-Kuhn model under the approximation of electric dipoles to the nonlinear situation by adding higher-order correction terms[3,44] yields

$$\frac{d^2u_1}{dt^2} + \gamma\frac{du_1}{dt} + \omega_0^2 u_1 + \xi u_2 + au_1^3 = -\frac{e}{m}A_x e^{-i\omega t + ik(z_0 + \frac{D}{2})} + \text{c.c.} \tag{1a}$$

$$\frac{d^2u_2}{dt^2} + \gamma\frac{du_2}{dt} + \omega_0^2 u_2 + \xi u_1 + au_2^3 = -\frac{e}{m}A_y e^{-i\omega t + ik(z_0 - \frac{D}{2})} + \text{c.c.} \tag{1b}$$

where u_1 and u_2 denote the displacement of the two oscillators from the equilibrium along the x and y directions, respectively, γ is the damping constant, ω_0 is the characteristic frequency of a single uncoupled oscillator, ξ is the coupling constant (which is a complex coefficient due to phase lag), a is the perturbation factor related to THG strength, e is the charge, m is the mass, z_0 is the central vertical position of the two oscillators, and D is the separation distance on the z axis. The abbreviation c.c. stands for complex conjugate. As fundamental incident light, we consider a plane wave propagating along the z direction with angular frequency ω and wave constant k in the propagation medium. The components of the incident electric field along x and y direction are denoted by A_x and A_y, respectively.

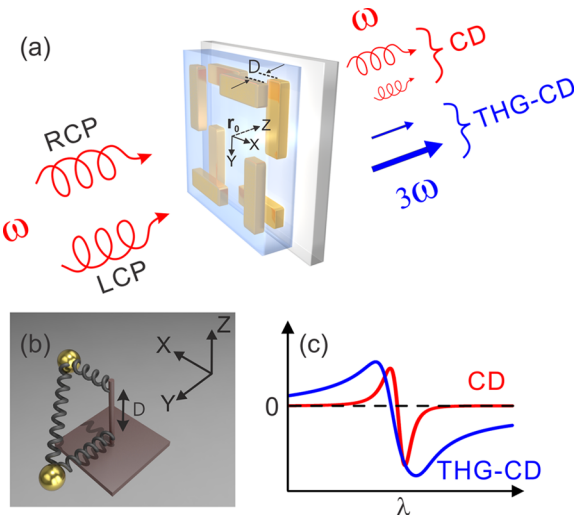

Figure 1. (a) Schematic plot of measuring linear (circular dichroism, CD) and nonlinear (third-harmonic-generation circular dichroism, THG-CD) chiroptical response of corner-stacked orthogonal gold nanorods arranged in C_4 symmetry. RCP: right-handed circular polarization, LCP: left-handed circular polarization. The coordinate system used in our model and the vertical distance between two layers are also shown. (b) Left-handed classical coupled oscillators for linear and nonlinear optical activity. (c) Sketch for linear and nonlinear circular dichroism response of a left-handed enantiomer plasmonic system.

According to perturbation theory,[38,45,46] u_1 and u_2 can be approximately expressed as the power series of perturbation parameter a, since the THG is very small compared to the unperturbed original terms

$$u_1 = u_1^{(1)} + au_1^{(3)} + o(a^2) \tag{2a}$$

$$u_2 = u_2^{(1)} + au_2^{(3)} + o(a^2) \tag{2b}$$

where $u_{1,2}^{(1)}$ are the unperturbed amplitudes of the plasmon oscillation that are attributed to the linear optical response, and $u_{1,2}^{(3)}$ are higher-order anharmonic amplitudes that contain the THG response and can be written as (see Supporting Information for details)

$$\begin{aligned} u_{1,2}^{(3)}(z_0, t, 3\omega) = {} & \frac{e^3}{m^3\omega_0^8}\{[F_+(3\omega)F_+^3(\omega) + F_-(3\omega)F_-^3(\omega)]A_{x,y}^3 \\ & \times e^{-i3\omega(t - \frac{Z_0 \pm \frac{D}{2}}{c})} \\ & + 3F_+(\omega)F_-(\omega)[F_+(3\omega)F_+(\omega) + F_-(3\omega)F_-(\omega)]A_{x,y}^2 A_{y,x} e^{-i3\omega(t - \frac{Z_0 \pm \frac{D}{6}}{c})} \\ & + 3F_+(\omega)F_-(\omega)[F_+(3\omega)F_-(\omega) + F_-(3\omega)F_+(\omega)]A_{x,y} A_{y,x}^2 e^{-i3\omega(t - \frac{Z_0 \mp \frac{D}{6}}{c})} \\ & + [F_+(3\omega)F_-^3(\omega) + F_-(3\omega)F_+^3(\omega)]A_{y,x}^3 e^{-i3\omega(t - \frac{Z_0 \mp \frac{D}{2}}{c})}\} + \text{c.c.} \end{aligned} \tag{3}$$

DOI: 10.1021/acsphotonics.9b01400
ACS Photonics 2019, 6, 3306−3314

with the linear response functions $F_+(\omega) = \omega_0^2(\omega_0^2 - \omega^2 - i\gamma\omega)/[(\omega_0^2 - \omega^2 - i\gamma\omega)^2 - \xi^2]$, and $F_-(\omega) = -\omega_0^2\xi/[(\omega_0^2 - \omega^2 - i\gamma\omega)^2 - \xi^2]$. The first subscripts of $A_{x,y}$ and $A_{y,x}$, together with the upper sign of $\pm$ and $\mp$ apply to $u_1^{(3)}$, while the second subscripts of $A_{x,y}$ and $A_{y,x}$, together with the lower sign of $\pm$ and $\mp$ apply to $u_2^{(3)}$. When taking C_4 rotational symmetry of the supercell into account, the third-order current density at arbitrary position $\boldsymbol{r} = (x,y,z)$, created by an ensemble of identical supercells, yields[38]

$$\boldsymbol{J}(\boldsymbol{r}, t, 3\omega) = -2aN_0e\left\{\boldsymbol{n_1}\left[\left.\frac{\mathrm{d}u_1^{(3)}(\boldsymbol{r_0}, t, 3\omega)}{\mathrm{d}t}\right|_{\boldsymbol{r_0}=\boldsymbol{r}-\boldsymbol{r}_1^{(0)}} - \left.\frac{\mathrm{d}u_2'^{(3)}(\boldsymbol{r_0}, t, 3\omega)}{\mathrm{d}t}\right|_{\boldsymbol{r_0}=\boldsymbol{r}-\boldsymbol{r}_2^{(0)}}\right] + \boldsymbol{n_2}\left[\left.\frac{\mathrm{d}u_2^{(3)}(\boldsymbol{r_0}, t, 3\omega)}{\mathrm{d}t}\right|_{\boldsymbol{r_0}=\boldsymbol{r}-\boldsymbol{r}_2^{(0)}} + \left.\frac{\mathrm{d}u_1'^{(3)}(\boldsymbol{r_0}, t, 3\omega)}{\mathrm{d}t}\right|_{\boldsymbol{r_0}=\boldsymbol{r}-\boldsymbol{r}_1^{(0)}}\right]\right\} \tag{4}$$

where N_0 denotes the supercell density of the structure, $\boldsymbol{n_1}$ and $\boldsymbol{n_2}$ are the unit vectors along the x and y directions, and $\boldsymbol{r_0} = (x_0,y_0,z_0)$ represents the center position of the supercell, with $\boldsymbol{r}_1^{(0)} = \left(0, 0, \frac{D}{2}\right)$ and $\boldsymbol{r}_2^{(0)} = \left(0, 0, -\frac{D}{2}\right)$. The relationship between $u'^{(3)}_{1,2}$ and $u^{(3)}_{1,2}$ can be described in such a fashion that if $u^{(3)}_{1,2} = f_{1,2}(A_x, A_y)$ is a function of electric-field amplitudes A_x and A_y, then we get $u'^{(3)}_{1,2} = f_{1,2}(A_y, -A_x)$ (see Supporting Information for details).

With $\boldsymbol{P}(\boldsymbol{r},t,3\omega) = \boldsymbol{J}(\boldsymbol{r},t,3\omega)/[-i(3\omega)]$, we obtain the third-order polarization components (the sources of THG intensity with $I_{\mathrm{THG}} \propto |\omega\cdot P|^2$)[46] in the following manner:

$$\begin{aligned} P_{x,y}(\boldsymbol{r}, t, 3\omega) = {} & \frac{-2N_0e^4a}{m^3\omega_0^8}\{2[F_+(3\omega)F_+^3(\omega) + F_-(3\omega)F_-^3(\omega)]A_{x,y}^3 \\ & + 3F_+(\omega)F_-(\omega)[F_+(3\omega)F_+(\omega) + F_-(3\omega)F_-(\omega)]A_{x,y}^2A_{y,x}(e^{\mp ikD} - e^{\pm ikD}) \\ & + 3F_+(\omega)F_-(\omega)[F_+(3\omega)F_-(\omega) + F_-(3\omega)F_+(\omega)]A_{x,y}A_{y,x}^2(e^{\mp 2ikD} + e^{\pm 2ikD}) \\ & + [F_+(3\omega)F_-^3(\omega) + F_-(3\omega)F_+^3(\omega)]A_{y,x}^3(e^{\mp 3ikD} - e^{\pm 3ikD})\}e^{-i(3\omega)t+i(3k)z} \\ & + \text{c.c.} \end{aligned} \tag{5}$$

Similar to the notation of eq 3, the first subscripts of $A_{x,y}$ and $A_{y,x}$, together with the upper sign of $\pm$ and $\mp$ apply to P_x, while the second subscripts of $A_{x,y}$ and $A_{y,x}$, together with the lower sign of $\pm$ and $\mp$ apply to P_y. Although eq 5 is lengthy, they help us to retrieve all the components of the third-order nonlinear susceptibility tensor very clearly. Furthermore, if the incident plane wave is circularly polarized, that is, $A_y = b\cdot A_x$, $b = \pm i$ (+ for LCP and − for RCP), then we obtain $P_y(\boldsymbol{r},t,3\omega) = (-b)\cdot P_x(\boldsymbol{r},t,3\omega)$. It indicates that the THG light remains circularly polarized, but exhibits reversed handedness compared to the fundamental light. Although our artificial chiral metamolecules are not significantly smaller in size than the wavelength of the studied light wave, we use the same procedure as in ref 38 that addresses the current density of natural molecules (see Chapter 8.3 of that reference). This worked reasonably well in our previous studies.[44,46,47] In addition, our conclusion of handedness reversion from fundamental wave to THG wave is in accordance with the rotational symmetry rule.[39] We emphasize that such a model can in principle be very powerful to explain the THG intensity with any fundamental plane wave exhibiting arbitrary states of polarization.

For retrieving the nonlinear CD signal from our model, we first measure the spectrally resolved transmission of our Born-Kuhn plasmonic nanorod arrays with LCP or RCP incidence. Then, the analytical expression for the linear CD (see eq 8 in ref 3) is used to fit the measured CD spectrum, from which we obtain the variables characterizing the properties of the oscillators such as γ, ω_0, and ξ. Together with the measured vertical separation D and the index of refraction of the embedding and spacer layer used in our experiment, eq 5 enables a prediction of the spectroscopic nonlinear yield with circularly polarized pump light, which results in the THG-CD [defined as $(\mathrm{THG_{LCP}} - \mathrm{THG_{RCP}})/(\mathrm{THG_{LCP}} + \mathrm{THG_{RCP}})$ in our paper, with the subscripts denoting the fundamental polarization states]. A similar procedure can be applied to the linear case, so that the absorbance of the plasmonic system with LCP and RCP incidence can be retrieved as well.[47] As depicted in Figure 1c, we are able in the end to compare the linear and nonlinear chiroptical response both in model and experiment. We would like to emphasize that the constants e, m, N_0, and a have the effect of a single proportionality coefficient which only contribute to the amplitudes of the linear and nonlinear fitting. They do not influence the relative differences between results with LCP or RCP pump light and hence play no role in THG-CD.

For linear and nonlinear measurements, we utilize a home-built femtosecond laser source together with a pulse shaper (PS), which delivers either broadband coherent light wave (supercontinuum, SC) or continuously tunable femtosecond pulses as the fundamental incidence (see the schematic picture in Figure 2a, with more details described in the Methods section). Nanofabrication procedures, including two-step electron-beam lithography, were performed in order to prepare either left- or right-handed enantiomers, see details in the Methods section. The scanning electron microscope (SEM) images of the enantiomorphic pairs are shown in Figure 2b and

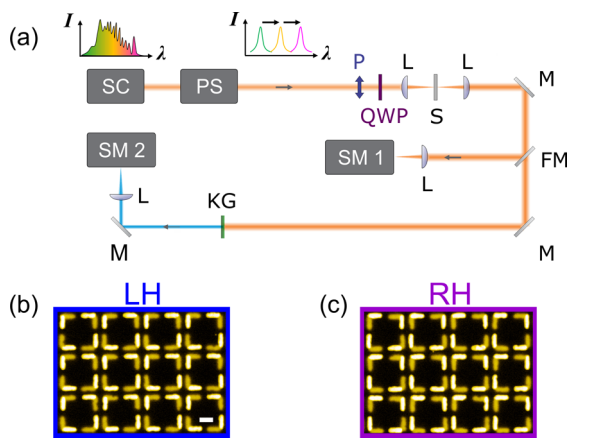

Figure 2. (a) Schematic picture of the measurement setup for both linear and nonlinear circular dichroism. SC: supercontinuum, PS: pulse shaper, P: polarizer, QWP: quarter waveplate, L: lens, S: sample/substrate, M: mirror, FM: flip mirror, SM: spectrometer, KG: KG filters. To measure linear optical chirality, a broadband supercontinuum and spectrometer 1 are used; to measure its nonlinear counterpart, the pulse shaper delivers 60 fs pulses in the spectral range from 960 to 1120 nm, and spectrometer 2 is employed to record third-harmonic generation. (b) Scanning electron microscope (SEM) image of a left-handed (LH) enantiomer. (c) SEM image of a right-handed (RH) enantiomer. The scale bar in the inset of (b) is 200 nm, and the same magnification is used in (b) and (c).

DOI: 10.1021/acsphotonics.9b01400
ACS Photonics 2019, 6, 3306−3314

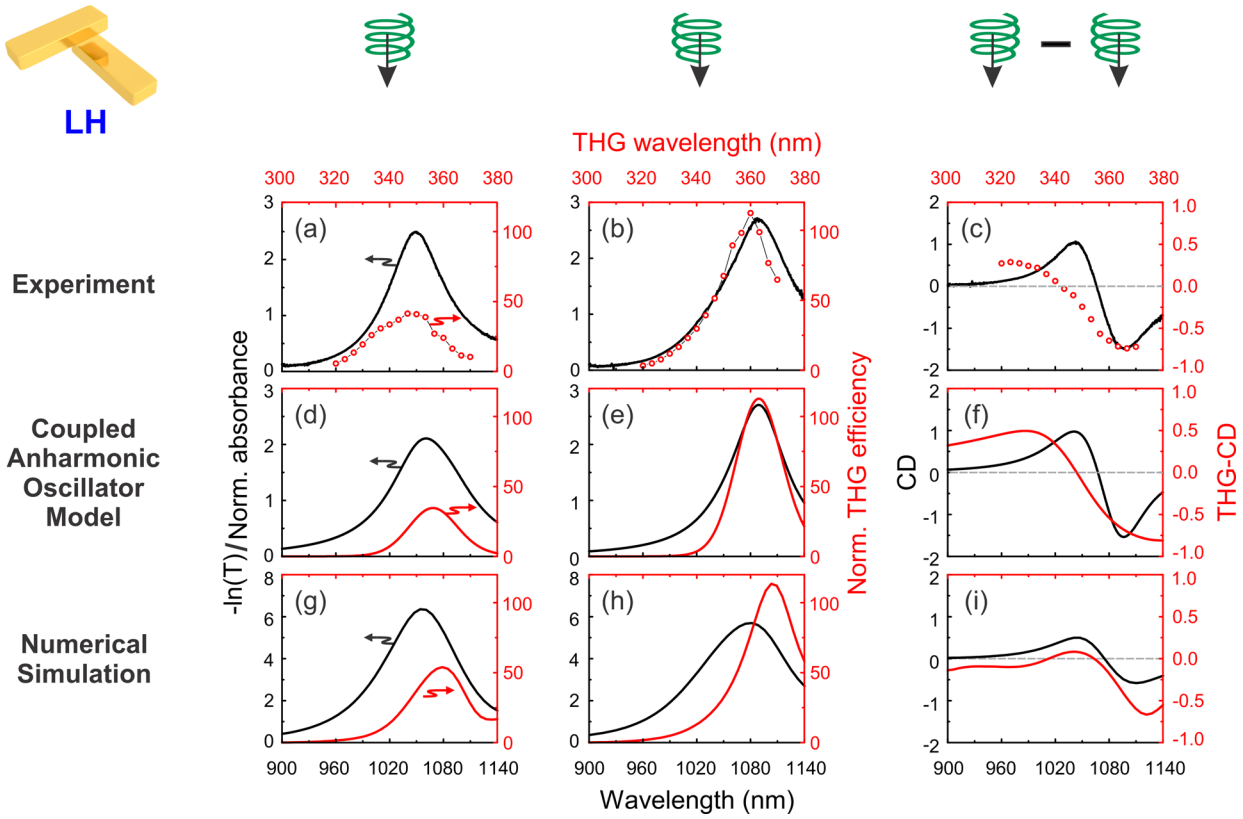

Figure 3. Measured (top row), modeled (middle row), and simulated (bottom row) linear (black) and nonlinear (red) chiroptical response of the left-handed enantiomer. The extinction [the negative logarithm of transmittance, $-\ln(T)$] and THG efficiency are displayed in (a), (d), and (g) for LCP and (b), (e), and (h) for RCP excitation schemes, and yield the CD and THG-CD shown in (c), (f), and (i). In the modeling, normalized absorbance instead of $-\ln(T)$ is given. The laser power is weak when the wavelength is tuned beyond the range from 960 to 1120 nm, so the corresponding THG results are too noisy to record, which leads to narrower spectral range of experimental data points (a–c) than modeled ones.

c, respectively. The structures are almost perfectly mirror symmetric and exhibit a periodicity in both directions of 600 nm, a rod length of 200 nm, a width of 70 nm, and a height of 40 nm. By using focused ion beam milling of a reference sample, we measured the thickness of the spacer layer to be about 110 nm.

We first characterize the linear and nonlinear CD for the LH enantiomer, as shown in Figure 3. Upon LCP illumination, the antibonding eigenmode can be excited much more efficiently, leading to a pronounced extinction peak at about 1050 nm, see the black curve in Figure 3a. In contrast, upon RCP illumination, the bonding eigenmode is located at a longer wavelength (about 1090 nm), denoted by the black curve in Figure 3b. The differential extinction, i.e., the CD, is represented in black in Figure 3c, which yields a bisignate profile with a maximum of about 1 and a minimum of about −1.5. The Born-Kuhn-type bilayer plasmonic metasurface exhibits many orders of magnitude larger optical activity than natural chiral molecules.[1,16,48] Among the chiral plasmonic nanostructures that have been studied before, its large chiral response stands out as well. Accordingly, the 3D gold nanorod arrays produce efficient THG signals together with remarkable THG-CD, see the red dots in Figure 3a–c. The nonlinear spectroscopic results almost follow those of the extinction spectra, that is, exhibit a maximum THG conversion efficiency near the corresponding resonance modes in both LCP and RCP excitation schemes (Figure 3a,b). This is reasonable from the viewpoint of near-field enhancement and coincides with other 2D nonlinear plasmonic systems.[46,49] More impressively, the nonlinear optical process seems to be much more efficient for a particular resonant eigenmode than the other (probably due to distinct quality factors of the two eigenmodes).[50,51] The difference of peak THG efficiency between LCP and RCP fundamental excitation is thus about 3-fold, much more significant than linear extinction, indicating that nonlinear optical activity is likely more sensitive to chirality (the handedness of either light or biomolecules) than its linear counterpart. Indeed the THG-CD is large, as demonstrated by the red dots in Figure 3c. It is bisignately distributed in the range of [−1, 1] and features a dip as large as −0.7, which is a remarkable value.[21] In addition, it is noteworthy that the maximum/minimum of THG-CD does not necessarily coincide with the same wavelength as that of the linear CD. In particular, in our case, at the wavelength where the linear CD exhibits a peak (about 1040 nm), the THG-CD nearly vanishes and might not be ideal for CD nonlinearities. To gain more fundamental insights into the nonlinear CD, we use the model as derived before. The modeled results are illustrated in Figure 3d–f (black curves for linear chiroptical response, and red dots for nonlinear chiroptical response). For the sake of better comparison, we normalize the modeled linear and THG results by two independent global parameters q_L and q_{NL} (they are connected with e, m, N_0, and so on in different manners), respectively. First the maximum absorbance and THG efficiency at RCP incidence are divided by constants q_L and q_{NL}, respectively, so that they can agree with the peak values of the experimental results. Then, the modeled absorbance and THG efficiency results at LCP incidence shown in Figure 3d

DOI: 10.1021/acsphotonics.9b01400
ACS Photonics 2019, 6, 3306−3314

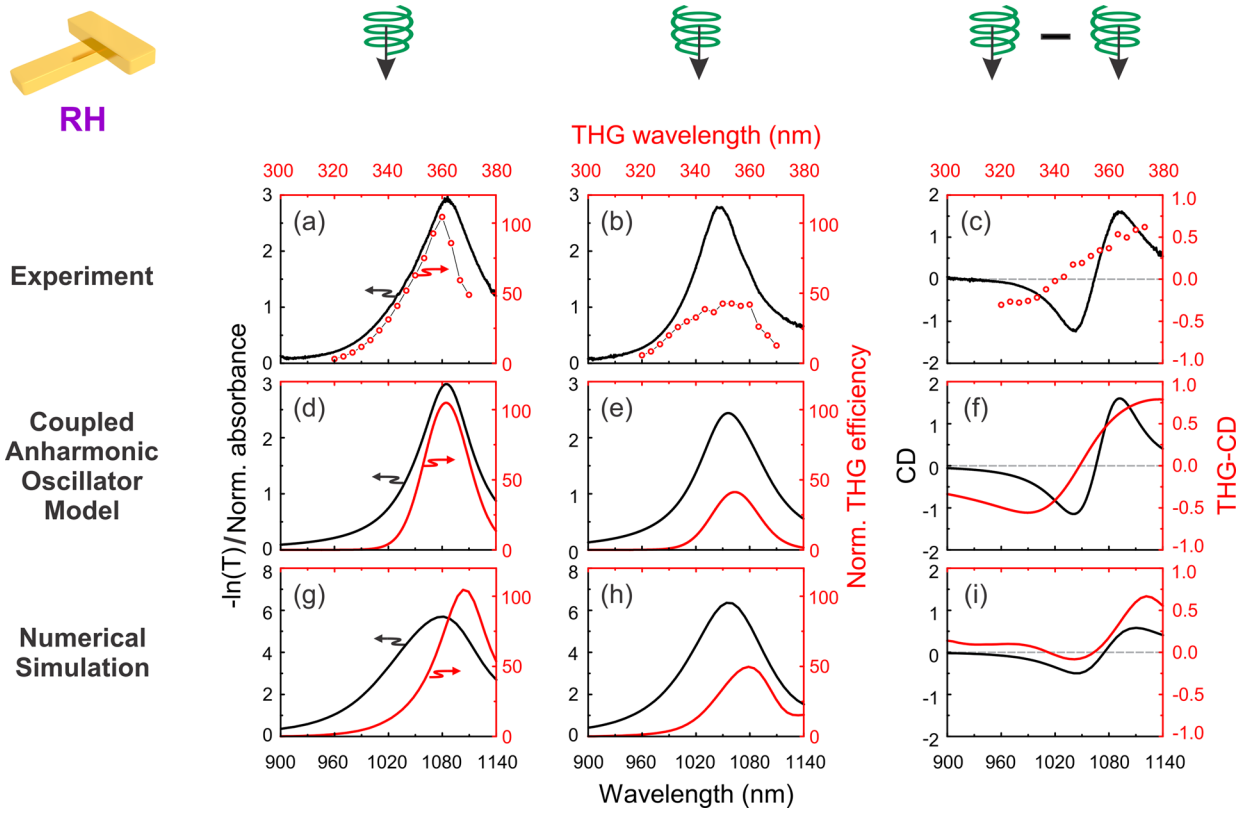

Figure 4. Measured (top row), modeled (middle row), and simulated (bottom row) linear (black) and nonlinear (red) chiroptical response of the right-handed enantiomer. The extinction and THG efficiency are displayed in (a), (d), and (g) for LCP and (b), (e), and (h) for RCP excitation schemes, and yield the CD and THG-CD shown in (c), (f), and (i).

are those divided by q_L and q_{NL}, respectively. To alleviate the fact that in our model (eq 5) we use a single-color continuous wave, while in our experiment we use 60 fs laser pulses with broader spectral bandwidth, we have taken moderate convolution effects from neighboring data points into account in our nonlinear modeling (see Supporting Information for more details). Regardless of this simplification, our nonlinear Born-Kuhn model gives good agreement when compared with the measurements, particularly in terms of the THG conversion efficiency difference between LCP and RCP excitation schemes. This confirms that our model is able to give the correct interpretation of THG-CD, as demonstrated in Figure 3f.

To further analyze the nonlinear chiroptical effects, we have additionally carried out full-field numerical simulations. Figure 3g–i is proof to the fact that our numerical simulations reveal the extinction and nonlinear yield both sensitively being dependent on the handedness of the pump wave, and both CD and THG-CD possess dispersive lineshapes. However, we find some disagreement to exist in comparison to our measurements. In detail, the CD and nonlinear CD seem to be smaller than in the experiment. One possible reason might arise from a mismatch between the imperfect structural nanofabrication in reality and the ideal lattice pattern in simulation, which could bring different coupling strength among ambient nanoparticles and hence different damping rates of the resonant modes. The spectral width of the bonding eigenmode is obviously larger in Figure 3h (black curve) than in both experiment and analytical model. In simulations, we additionally observe that the most efficient nonlinear emission occurs at a more red-shifted wavelength than in measurement. The redshift feature of nonlinear peak position with respect to its linear extinction could be related to the damping-induced difference between near and far fields[52] and might be amplified by perfect structural assumption in our simulations.

Similarly, we have performed linear and nonlinear CD measurements for the RH enantiomer, in combination with analytical modeling and numerical simulation, see Figure 4. For an ideally mirror symmetric chiral object, one would expect that its optical behavior rigorously reverses with the chirality of excitation light in comparison to that of the other handedness. Due to our minute nanofabrication errors, the RH nanostructures here are slightly different in dimension, leading to observable differences in their chiral optical response compared to the LH enantiomer (spectral position, width, and amplitude of the resonances). Hence the THG response is not perfectly reversed with handedness of pump light as well. In the model, however, we are capable of considering the dimensional discrepancy by fitting the actually measured CD spectrum, from which different oscillator parameters are extracted and well suited to predict the measured THG-CD. Our model also works well for Born-Kuhn-type gold nanostructures resonant at different spectral windows, see details in Figure S3 of the Supporting Information. It reflects the capability of the model to predict the nonlinear chiroptical response based on measurements of its linear counterpart. Again, numerical simulations have been performed, yielding perfectly reversed results (Figure 4g–i) of chirality of fundamental light in comparison to the LH enantiomer.

Ideally, the nonlinear Born-Kuhn model can also be used to interpret the THG intensity at arbitrary states of incident polarization. By experimentally rotating the QWP in front of

DOI: 10.1021/acsphotonics.9b01400
ACS Photonics 2019, 6, 3306–3314

our samples, we generate a series of polarized fundamental light with varying ellipticity. By adding an analyzer after the nonlinear light generation, we can measure the amplitude of s and p components of the THG waves ($THG^{s,p}$), where the s-polarization is defined to be vertical with respect to our optical table plane (namely, s-polarization is along the *Y* axis shown in Figure 1). The experimental configuration is depicted in Figure 5a. Measurement was taken from the LH enantiomer at the

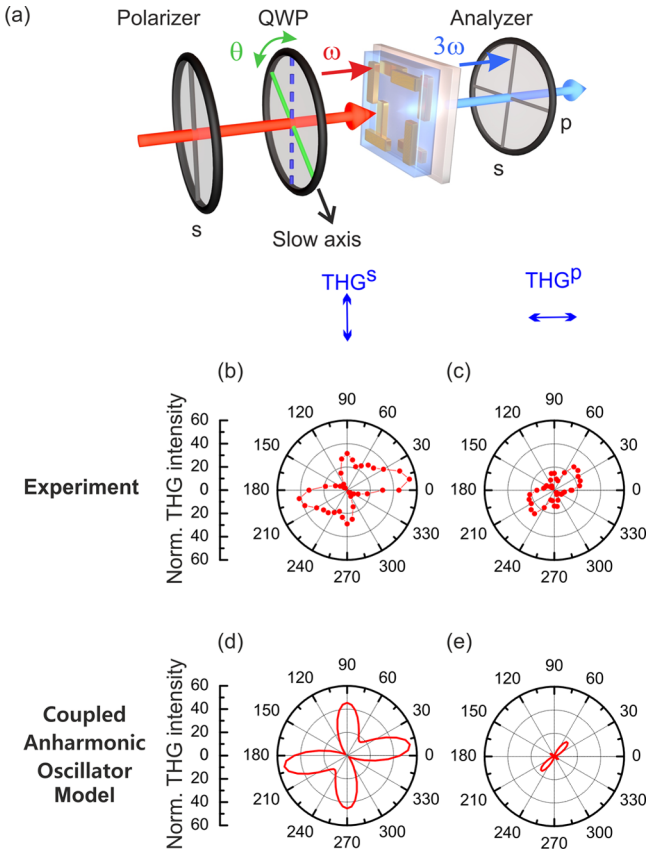

Figure 5. Measured (middle row) and modeled (bottom row) s- and p-polarized THG efficiency (THG^s, THG^p) as a function of the polarization state of fundamental light (illustrated as a function of rotational angle of QWP θ in degrees). (a) Experimental configuration, where s-polarization is along the *Y*-axis shown in Figure 1, and θ is the angle of the QWP slow axis with respect to s-polarization. The fundamental laser at the central wavelength of 1100 nm is sent to the left-handed enantiomer. (b, d) The s-component of the THG light, and (c, e) the p-component of the THG light.

wavelength of 1100 nm. All THG intensity is normalized to that of substrate when using s-polarized fundamental light and measuring s-polarized THG light. As shown by the polar-plot patterns in Figure 5b,c, both THG^s and THG^p exhibit two maxima and two minima within one cycle (when θ varies from 0 to 180°), which can be well reproduced within the second cycle (from 180 to 360°, generating the same fundamental polarization states as the first cycle). Interestingly, the maximum THG^s intensity is several times larger than the maximum THG^p intensity. Our nonlinear model predicts to a large extent similar patterns to the experiment for both THG^s and THG^p, in addition to the efficiency difference of the two components (see Figure 5d,e; the modeled THG intensity is normalized such that the maximum THG^s intensity is equal to that in the experiment). One can still find, however, some disagreement between experiment and model. Particularly, although our model (as well as the numerical simulations) predicts a perfectly reversed handedness of THG light with respect to fundamental light, the samples do not generate purely circularly polarized THG light upon circularly polarized fundamental light (see more details in Figure S4 and Table S1). The state of polarization of the THG light in the experiment seems to be extremely sensitive to wavelength, exact sample geometry, and so on. The reasons could be manifold: First, our broadband QWP does not give exactly $\pi/2$ retardance at every wavelength. Furthermore, the laser beam is always focused at a finite numerical aperture onto our samples. Both aspects render it difficult to warrant generation of purely circularly polarized fundamental plane waves. Second, the fabricated nanostructures include some minor defects and are not exactly C_4 symmetrical. Due to the nonlinear proportionality, the aforementioned imperfections can even be amplified in the THG process. Third, our model is very simplified and limited. Especially, our artificial chiral substances are not as microscopically small as natural chiral molecules due to their finite size. In addition, the two corner-stacked orthogonal gold nanorods themselves as a unit are not C_4 symmetrical, which are not significantly smaller in size when compared to the optical wavelength. All these factors contribute and might cause difficulties when considering the expected absence of SHG generation as well (see Figure S6 as an example).

CONCLUSION

In conclusion, we have investigated THG-CD of the archetypical Born-Kuhn-type plasmonic analog made of 3D gold chiral metasurfaces in experiment, analytical coupled anharmonic oscillator model, and numerical full-field simulation. Our experiment constitutes a classical system to assess linear and nonlinear chiroptical effects induced by chirally arranged electric dipoles. The nonlinear coupled anharmonic oscillator model considers both spatial phase retardation of the 3D plasmonic nanostructures and arrangement symmetry, enabling analysis of the nonlinear susceptibility tensors that determine the THG-CD. The quantitative comparison between CD and THG-CD indicates that despite similar spectral profiles, linear and nonlinear CD can exhibit maximum or minimum value at distinct wavelengths. In particular, at the spectral position where the linear CD peaks, the nonlinear CD is actually close to zero. Our plasmonic metamolecules also show broader peak and dip of the THG-CD spectra than those of linear CD spectra. Since we might choose the peak or dip positions for sensitive chiral sensing, it is highly instructive to know and understand the differences between the nonlinear CD and its linear counterpart beforehand.

It might be surprising that the nonlinear optical behavior of such a complex chiral system can be described by rather simple coupled anharmonic oscillators. Nevertheless, it turns out that such an analytical model is able to capture the related physics and interpret the main spectral features. Our method might be applied to analysis of chiroptical response from other 3D chiral plasmonic systems such as vertically coupled bilayer nanorods arranged in C_3 symmetry, which also avoids linear birefringence.[10] It may be also helpful to understand more sophisticated 3D plasmonic nanostructures, in which single uncoupled particles are resonant at different eigenfrequencies, in the case of so-called constitution-induced chirality.[1] Our work could pave an avenue toward tailoring and designing nonlinear optical behavior in complex artificial chiral plasmonic

DOI: 10.1021/acsphotonics.9b01400
ACS Photonics 2019, 6, 3306−3314

metamolecules, which might be suitable for applications in biosensing and imaging.

METHODS

Optical Measurements. The nonlinear spectroscopy was performed by using 60 fs transform-limited Gaussian pulses. The central wavelength was scanned from 960 to 1120 nm, with a tuning step of 10 nm. The average power of the laser pulses was attenuated to about 15 mW for the safety of the samples, and the repetition rate is 44 MHz. A polarizer (P) and a quarter waveplate (QWP) are added afterward to generate circularly or elliptically polarized light. The laser beam is focused onto our samples (S) at normal incidence via an achromatic lens (L) with a focal length of 75 mm, which produces a beam waist diameter of about 50 μm. The transmitted light is recollimated by another lens and sent into spectrometer 1 (SM1, Ando AQ6317) through several reflective mirrors (M) and an additional focus lens. For THG detection, the flip mirror (FM) is switched such that the THG signal radiated in forward direction can enter the other spectrometer (SM2, Princeton Instruments Acton SP2500) after a series of KG filters from Schott block efficiently the fundamental light. The THG wave is dispersed by a grating inside SM2 and then recorded by a CCD detector (Princeton Instruments PIXIS 256). For a given central wavelength when spectrally sweeping the pump laser, we fit the entire THG spectrum under the assumption of a Gaussian spectral shape and then integrate it spectrally to obtain an overall THG conversion efficiency at that particular fundamental wavelength. For normalization in both linear and nonlinear configurations, we shine light onto our glass substrate (Suprasil) and record the corresponding transmittance and THG intensity. Since the substrate is amorphous and isotropic, we always record its THG light using a linearly polarized fundamental wave. The polarization sensitivity of our setup such as polarization-dependent diffraction efficiency of the grating in SM2 is not pronounced, as confirmed by our previous work,[44,49] and is hence neglected in this work.

Nanostructure Fabrication. The Born-Kuhn plasmonic analog consisting of corner-stacked orthogonal gold nanorods arranged in C_4 symmetry was fabricated by a two-step electron-beam lithography (EBL) technique in combination with a precision alignment procedure. First, the glass substrate is covered by a dielectric spacer layer (IC1−200, Futurrex) via spin-coating. Second, EBL processing procedures (electron-beam exposure of a PMMA resist, development, evaporation of a gold film, and subsequent lift-off) are implemented to fabricate one layer of gold nanorods. The rod lengths were finely varied and optimized in order to tailor their plasmonic resonances within the spectral range of our ultrafast laser source. Third, another IC1−200 spacer layer is spin-coated above the layer of gold nanoparticles. Fourth, employing a second EBL cycle assisted by precise positioning, the second layer of gold nanorods is finished. Finally, a third IC1−200 spacer layer is planarized on top in order to create an isotropic environment for the gold nanostructures. For complete spectroscopic measurements, the dimensional parameters of gold nanorods together with the thickness of the IC1−200 spacer layer were optimized, which ensures large resonant optical activity and simultaneously allows for two eigenmodes to be both resonant within the spectral range of our ultrafast laser source. Our reproducible experimental measurement of both linear and nonlinear optical activity from duplicate samples as those in Figures 3 and 4 indicates the high reliability of the nanofabrication (Supporting Information).

Numerical Simulations. For the linear simulations, an implementation of the Fourier modal method has been used.[42,53] In our simulation, the refractive indices of glass and IC1−200 are taken as 1.46 and 1.3, respectively. The permittivity of gold was calculated using the critical point model.[54] For the nonlinear simulations, our approach is as follows: First, the electric fields at the fundamental wavelength are calculated by the Fourier modal method under the assumption that any self-phase modulation can be neglected. Then, we use these fields and Miller's rule[45] to calculate the third-order nonlinear polarization within the undepleted pump approximation.[43,55] The nonlinear polarization acts as a source at the third-harmonic wavelength.[43,55,56] However, instead of calculating the direct emission problem,[57] we make use of the reciprocity principle[58,59] and calculate the near fields for p- and s-polarized plane waves incident from the far fields at the third-harmonic wavelength. Then, the electric field radiated to the far field at the third harmonic can be calculated as the overlap integral of these near fields and the nonlinear source.[43,55]

ASSOCIATED CONTENT

Supporting Information

The Supporting Information is available free of charge at https://pubs.acs.org/doi/10.1021/acsphotonics.9b01400.

> Detailed derivation of nonlinear Born-Kuhn model and plot of calculated current density in full-field simulations; linear and nonlinear chiroptical spectroscopy of Born-Kuhn-type plasmonic nanostructures resonant at longer wavelengths; polarization state of THG light; experimental spectroscopic results for duplicate samples; comparison of THG and SHG intensity; the influence of spectral bandwidth of fundamental wave in nonlinear modeling (PDF)

AUTHOR INFORMATION

Corresponding Author

*E-mail: liligui@bupt.edu.cn.

ORCID

Lili Gui: 0000-0002-3710-6330

Joachim Krauth: 0000-0001-9683-762X

Thomas Weiss: 0000-0002-4991-6779

Notes

The authors declare no competing financial interest.

ACKNOWLEDGMENTS

The authors gratefully acknowledge financial support from the European Research Council (ERC Advanced Grant Complex-Plas), Bundesministerium für Bildung and Forschung, Deutsche Forschungsgemeinschaft (SPP1391 and 1839), Baden-Württemberg Stiftung, Ministerium für Wissenschaft, Forschung und Kunst Baden-Württemberg (ZAQuant, IQST), VW Foundation, and Carl-Zeiss Foundation. L.G. additionally acknowledges funding from the National Natural Science Foundation of China (Grant No. 61905018), Fund of State Key Laboratory of Information Photonics and Optical Communications (Beijing University of Posts and Telecommunications) of China (IPOC2019ZT04), Beijing Nova Program, and the Fundamental Research Funds for the Central Universities from China (2019RC14). The authors thank Dr.

DOI: 10.1021/acsphotonics.9b01400
ACS Photonics 2019, 6, 3306−3314

Song Yue and Dr. Xinghui Yin for valuable discussion and structural fabrication in an early stage of the experiment. Also, we would like to thank Dr. Bernd Metzger and Dr. Nikolai Strohfeldt for their important measurement support. In addition, the assistance with numerical simulations from Dr. Martin Schäferling is greatly appreciated.

REFERENCES

(1) Hentschel, M.; Schäferling, M.; Duan, X.; Giessen, H.; Liu, N. Chiral plasmonics. *Sci. Adv.* **2017**, *3*, No. e1602735.
(2) Valev, V. K.; Baumberg, J. J.; Sibilia, C.; Verbiest, T. Chirality and chiroptical effects in plasmonic nanostructures: fundamentals, recent progress, and outlook. *Adv. Mater.* **2013**, *25*, 2517−2534.
(3) Yin, X.; Schäferling, M.; Metzger, B.; Giessen, H. Interpreting chiral nanophotonic spectra: the plasmonic Born-Kuhn model. *Nano Lett.* **2013**, *13*, 6238−6243.
(4) Fischer, P.; Hache, F. Nonlinear optical spectroscopy of chiral molecules. *Chirality* **2005**, *17*, 421−437.
(5) Kuzyk, A.; Schreiber, R.; Zhang, H.; Govorov, A. O.; Liedl, T.; Liu, N. Reconfigurable 3D plasmonic metamolecules. *Nat. Mater.* **2014**, *13*, 862−866.
(6) Liu, N.; Liedl, T. DNA-assembled advanced plasmonic architectures. *Chem. Rev.* **2018**, *118*, 3032−3053.
(7) Decker, M.; Ruther, M.; Kriegler, C.; Zhou, J.; Soukoulis, C.; Linden, S.; Wegener, M. Strong optical activity from twisted-cross photonic metamaterials. *Opt. Lett.* **2009**, *34*, 2501−2503.
(8) Schäferling, M.; Dregely, D.; Hentschel, M.; Giessen, H. Tailoring enhanced optical chirality: design principles for chiral plasmonic nanostructures. *Phys. Rev. X* **2012**, *2*, 031010.
(9) Schäferling, M.; Engheta, N.; Giessen, H.; Weiss, T. Reducing the complexity: Enantioselective chiral near-fields by diagonal slit and mirror configuration. *ACS Photonics* **2016**, *3*, 1076−1084.
(10) Hentschel, M.; Schäferling, M.; Weiss, T.; Liu, N.; Giessen, H. Three-dimensional chiral plasmonic oligomers. *Nano Lett.* **2012**, *12*, 2542−2547.
(11) Poulikakos, L. V.; Gutsche, P.; McPeak, K. M.; Burger, S.; Niegemann, J.; Hafner, C.; Norris, D. J. Optical chirality flux as a useful far-field probe of chiral near fields. *ACS Photonics* **2016**, *3*, 1619−1625.
(12) Poulikakos, L. V.; Thureja, P.; Stollmann, A.; De Leo, E.; Norris, D. J. Chiral light design and detection inspired by optical antenna theory. *Nano Lett.* **2018**, *18*, 4633−4640.
(13) Garcia-Guirado, J.; Rica, R. A.; Ortega, J.; Medina, J.; Sanz, V.; Ruiz-Reina, E.; Quidant, R. Overcoming diffusion-limited biosensing by electrothermoplasmonics. *ACS Photonics* **2018**, *5*, 3673−3679.
(14) Baffou, G.; Quidant, R. Nanoplasmonics for chemistry. *Chem. Soc. Rev.* **2014**, *43*, 3898−3907.
(15) Zhao, Y.; Askarpour, A. N.; Sun, L.; Shi, J.; Li, X.; Alù, A. Chirality detection of enantiomers using twisted optical metamaterials. *Nat. Commun.* **2017**, *8*, 14180.
(16) Hendry, E.; Carpy, T.; Johnston, J.; Popland, M.; Mikhaylovskiy, R.; Lapthorn, A.; Kelly, S.; Barron, L.; Gadegaard, N.; Kadodwala, M. Ultrasensitive detection and characterization of biomolecules using superchiral fields. *Nat. Nanotechnol.* **2010**, *5*, 783−787.
(17) Garcia-Guirado, J.; Svedendahl, M.; Puigdollers, J.; Quidant, R. Enantiomer-Selective Molecular Sensing Using Racemic Nanoplasmonic Arrays. *Nano Lett.* **2018**, *18*, 6279−6285.
(18) Valev, V.; Silhanek, A.; Verellen, N.; Gillijns, W.; Van Dorpe, P.; Aktsipetrov, O.; Vandenbosch, G.; Moshchalkov, V.; Verbiest, T. Asymmetric optical second-harmonic generation from chiral G-shaped gold nanostructures. *Phys. Rev. Lett.* **2010**, *104*, 127401.
(19) Huttunen, M. J.; Bautista, G.; Decker, M.; Linden, S.; Wegener, M.; Kauranen, M. Nonlinear chiral imaging of subwavelength-sized twisted-cross gold nanodimers. *Opt. Mater. Express* **2011**, *1*, 46−56.
(20) Ren, M.; Plum, E.; Xu, J.; Zheludev, N. I. Giant nonlinear optical activity in a plasmonic metamaterial. *Nat. Commun.* **2012**, *3*, 833.
(21) Valev, V. K.; Baumberg, J.; De Clercq, B.; Braz, N.; Zheng, X.; Osley, E.; Vandendriessche, S.; Hojeij, M.; Blejean, C.; Mertens, J.; et al. Nonlinear superchiral metasurfaces: tuning chirality and disentangling nonreciprocity at the Nanoscale. *Adv. Mater.* **2014**, *26*, 4074−4081.
(22) Kolkowski, R.; Petti, L.; Rippa, M.; Lafargue, C.; Zyss, J. Octupolar plasmonic meta-molecules for nonlinear chiral watermarking at subwavelength scale. *ACS Photonics* **2015**, *2*, 899−906.
(23) Chen, S.; Zeuner, F.; Weismann, M.; Reineke, B.; Li, G.; Valev, V. K.; Cheah, K. W.; Panoiu, N. C.; Zentgraf, T.; Zhang, S. Giant nonlinear optical activity of achiral origin in planar metasurfaces with quadratic and cubic nonlinearities. *Adv. Mater.* **2016**, *28*, 2992−2999.
(24) Collins, J. T.; Hooper, D. C.; Mark, A. G.; Kuppe, C.; Valev, V. K. Second Harmonic Generation Optical Rotation Solely Attributable to Chirality in Plasmonic Metasurfaces. *ACS Nano* **2018**, *12*, 5445−5451.
(25) Byers, J.; Yee, H.; Hicks, J. A second harmonic generation analog of optical rotatory dispersion for the study of chiral monolayers. *J. Chem. Phys.* **1994**, *101*, 6233−6241.
(26) Mesch, M.; Metzger, B.; Hentschel, M.; Giessen, H. Nonlinear plasmonic sensing. *Nano Lett.* **2016**, *16*, 3155−3159.
(27) Butet, J.; Martin, O. J. Nonlinear plasmonic nanorulers. *ACS Nano* **2014**, *8*, 4931−4939.
(28) Kravtsov, V.; Ulbricht, R.; Atkin, J. M.; Raschke, M. B. Plasmonic nanofocused four-wave mixing for femtosecond near-field imaging. *Nat. Nanotechnol.* **2016**, *11*, 459−464.
(29) Linden, S.; Niesler, F.; Förstner, J.; Grynko, Y.; Meier, T.; Wegener, M. Collective effects in second-harmonic generation from split-ring-resonator arrays. *Phys. Rev. Lett.* **2012**, *109*, 015502.
(30) Obermeier, J.; Schumacher, T.; Lippitz, M. Nonlinear spectroscopy of plasmonic nanoparticles. *Adv. Phys. X* **2018**, *3*, 1454341.
(31) Valev, V.; Smisdom, N.; Silhanek, A.; De Clercq, B.; Gillijns, W.; Ameloot, M.; Moshchalkov, V.; Verbiest, T. Plasmonic ratchet wheels: switching circular dichroism by arranging chiral nanostructures. *Nano Lett.* **2009**, *9*, 3945−3948.
(32) Rodrigues, S. P.; Lan, S.; Kang, L.; Cui, Y.; Cai, W. Nonlinear imaging and spectroscopy of chiral metamaterials. *Adv. Mater.* **2014**, *26*, 6157−6162.
(33) Kang, L.; Lan, S.; Cui, Y.; Rodrigues, S. P.; Liu, Y.; Werner, D. H.; Cai, W. An active metamaterial platform for chiral responsive optoelectronics. *Adv. Mater.* **2015**, *27*, 4377−4383.
(34) Hooper, D. C.; Mark, A. G.; Kuppe, C.; Collins, J. T.; Fischer, P.; Valev, V. K. Strong rotational anisotropies affect nonlinear chiral metamaterials. *Adv. Mater.* **2017**, *29*, 1605110.
(35) Mark, A. G.; Gibbs, J. G.; Lee, T.-C.; Fischer, P. Hybrid nanocolloids with programmed three-dimensional shape and material composition. *Nat. Mater.* **2013**, *12*, 802−807.
(36) Gibbs, J. G.; Mark, A. G.; Lee, T.-C.; Eslami, S.; Schamel, D.; Fischer, P. Nanohelices by shadow growth. *Nanoscale* **2014**, *6*, 9457−9466.
(37) Kuhn, W. The physical significance of optical rotatory power. *Trans. Faraday Soc.* **1930**, *26*, 293−308.
(38) Svirko, Y. P.; Zheludev, N. I. *Polarization of Light in Nonlinear Optics*; John Wiley & Sons: New York, 1998.
(39) Chen, S.; Li, G.; Zeuner, F.; Wong, W. H.; Pun, E. Y. B.; Zentgraf, T.; Cheah, K. W.; Zhang, S. Symmetry-selective third-harmonic generation from plasmonic metacrystals. *Phys. Rev. Lett.* **2014**, *113*, 033901.
(40) Li, G.; Chen, S.; Pholchai, N.; Reineke, B.; Wong, P. W. H.; Pun, E. Y. B.; Cheah, K. W.; Zentgraf, T.; Zhang, S. Continuous control of the nonlinearity phase for harmonic generations. *Nat. Mater.* **2015**, *14*, 607−612.
(41) Li, G.; Zentgraf, T.; Zhang, S. Rotational Doppler effect in nonlinear optics. *Nat. Phys.* **2016**, *12*, 736−740.
(42) Weiss, T.; Granet, G.; Gippius, N. A.; Tikhodeev, S. G.; Giessen, H. Matched coordinates and adaptive spatial resolution in the Fourier modal method. *Opt. Express* **2009**, *17*, 8051−8061.

DOI: 10.1021/acsphotonics.9b01400
ACS Photonics 2019, 6, 3306−3314

(43) O'Brien, K.; Suchowski, H.; Rho, J.; Salandrino, A.; Kante, B.; Yin, X.; Zhang, X. Predicting nonlinear properties of metamaterials from the linear response. *Nat. Mater.* **2015**, *14*, 379−383.
(44) Metzger, B.; Hentschel, M.; Nesterov, M.; Schumacher, T.; Lippitz, M.; Giessen, H. Nonlinear optics of complex plasmonic structures: linear and third-order optical response of orthogonally coupled metallic nanoantennas. *Appl. Phys. B: Lasers Opt.* **2016**, *122*, 77.
(45) Boyd, R. W. *Nonlinear Optics*, 2nd ed.; Academic Press: Amsterdam, 2003.
(46) Metzger, B.; Hentschel, M.; Lippitz, M.; Giessen, H. Third-harmonic spectroscopy and modeling of the nonlinear response of plasmonic nanoantennas. *Opt. Lett.* **2012**, *37*, 4741−4743.
(47) Hentschel, M.; Utikal, T.; Giessen, H.; Lippitz, M. Quantitative modeling of the third harmonic emission spectrum of plasmonic nanoantennas. *Nano Lett.* **2012**, *12*, 3778−3782.
(48) Ghosh, A.; Fischer, P. Chiral molecules split light: reflection and refraction in a chiral liquid. *Phys. Rev. Lett.* **2006**, *97*, 173002.
(49) Gui, L.; Bagheri, S.; Strohfeldt, N.; Hentschel, M.; Zgrabik, C. M.; Metzger, B.; Linnenbank, H.; Hu, E. L.; Giessen, H. Nonlinear refractory plasmonics with titanium nitride nanoantennas. *Nano Lett.* **2016**, *16*, 5708−5713.
(50) Metzger, B.; Hentschel, M.; Schumacher, T.; Lippitz, M.; Ye, X.; Murray, C. B.; Knabe, B.; Buse, K.; Giessen, H. Doubling the efficiency of third harmonic generation by positioning ITO nanocrystals into the hot-spot of plasmonic gap-antennas. *Nano Lett.* **2014**, *14*, 2867−2872.
(51) Metzger, B.; Schumacher, T.; Hentschel, M.; Lippitz, M.; Giessen, H. Third harmonic mechanism in complex plasmonic Fano structures. *ACS Photonics* **2014**, *1*, 471−476.
(52) Zuloaga, J.; Nordlander, P. On the energy shift between near-field and far-field peak intensities in localized plasmon systems. *Nano Lett.* **2011**, *11*, 1280−1283.
(53) Weiss, T.; Gippius, N. A.; Tikhodeev, S. G.; Granet, G.; Giessen, H. Derivation of plasmonic resonances in the Fourier modal method with adaptive spatial resolution and matched coordinates. *J. Opt. Soc. Am. A* **2011**, *28*, 238−244.
(54) Etchegoin, P. G.; Le Ru, E.; Meyer, M. An analytic model for the optical properties of gold. *J. Chem. Phys.* **2006**, *125*, 164705.
(55) Nesterov, M.; Schäferling, M.; Weber, K.; Neubrech, F.; Giessen, H.; Weiss, T. Line-current model for deriving the wavelength scaling of linear and nonlinear optical properties of thin elongated metallic rod antennas. *J. Opt. Soc. Am. B* **2018**, *35*, 1482−1489.
(56) Defrance, J.; Schäferling, M.; Weiss, T. Modeling of second-harmonic generation in periodic nanostructures by the Fourier modal method with matched coordinates. *Opt. Express* **2018**, *26*, 13746−13758.
(57) Lobanov, S.; Weiss, T.; Dregely, D.; Giessen, H.; Gippius, N.; Tikhodeev, S. Emission properties of an oscillating point dipole from a gold Yagi-Uda nanoantenna array. *Phys. Rev. B: Condens. Matter Mater. Phys.* **2012**, *85*, 155137.
(58) Weiss, T.; Muljarov, E. How to calculate the pole expansion of the optical scattering matrix from the resonant states. *Phys. Rev. B: Condens. Matter Mater. Phys.* **2018**, *98*, 085433.
(59) Yang, J.; Hugonin, J.-P.; Lalanne, P. Near-to-far field transformations for radiative and guided waves. *ACS Photonics* **2016**, *3*, 395−402.

DOI: 10.1021/acsphotonics.9b01400
ACS Photonics 2019, 6, 3306−3314